Progress in Flight Physics **7** (2015) 311-328
DOI: 10.1051/eucass/201507311

COMBINED EXPERIMENTAL AND NUMERICAL INVESTIGATION OF A TRANSONIC SPACE LAUNCHER WAKE

S. Scharnowski[1], V. Statnikov[2], M. Meinke[2], W. Schröder[2], and C. J. Kähler[1]

[1]Institute of Fluid Mechanics and Aerodynamics
Bundeswehr University Munich
Munich, Germany

[2]Institute of Aerodynamics
RWTH Aachen University
Aachen, Germany

Combined experimental und numerical investigations of the turbulent wake of a generic space launcher at transonic free stream conditions ($Ma_\infty = 0.7$ and $Re_D = 1.0 \cdot 10^6$) are performed to gain a better understanding of intricate phenomena of the wake flow physics and to validate new methods for its analysis. The experiments are conducted at the Bundeswehr University Munich using a high-repetition-rate particle image velocimetry (PIV) system, while the numerical investigation is performed by the Institute of Aerodynamics of RWTH Aachen University using a zonal Reynolds-averaged Navier–Stokes (RANS) / large-eddy simulation (LES) approach. After a characterization of the wake flow topology, two applied methodologies are compared to each other with respect to the spatial and temporal resolution stressing their strengths and shortcomings. It is shown that both methods are well suitable for the prediction of the mean and instantaneous values of the turbulent velocity field, whereas for a reliable statistical analysis of the velocity fluctuations, the PIV approach is more appropriate due to the computational time limitations of the LES. On the other hand, the high spatial and temporal resolution of the LES allows for an accurate detection of relevant coherent structures as well as tracking their motion in time without any significant artificial vortex agglomeration that can be critical in the case of PIV. Furthermore, the influence of different model assumptions, e. g., the level of incoming turbulence and model vibrations, is discussed in order to emphasize the importance of a side-by-side combination of both investigation techniques.

1 INTRODUCTION

The presented results are obtained within the framework of the German Transregional Collaborative Research Center TRR 40 founded by the German Research Foundation which focuses on the analysis and modeling of coupled liquid rocket propulsion systems and their integration into the space transportation system. The overall objective is to develop technological foundations for the design of thermally and mechanically highly loaded components of future space transportation systems, one of which is the wake flow. Although in most cases the space launcher base geometry is quite simple, the wake flow field is determined by different phenomena, such as flow separation at the base shoulder, reattachment of the shear layer at the outer nozzle wall, interaction with the jet plume, to name a few. Particularly, the reattachment of the shed shear layer causes strong wall pressure fluctuations which lead to increased dynamic loads on the nozzle structure [1]. The loads are the strongest in the transonic regime and the characteristic frequencies of the pressure fluctuations may interfere with the structural modes of the nozzle leading to so-called buffeting. Hannemann *et al.* [2] as well as Schrijer *et al.* [3] showed that shedding of large wake vortices is the driving force for the aerodynamic unsteady phenomena. Therefore, an accurate prediction of interaction between the shear layer and the nozzle in the wake of the launcher is particularly important. For the design of next generation space launchers, it is essential, on the one hand, to develop efficient and reliable numerical tools and, on the other hand, to achieve accurate experimental results with sufficiently high spatial and temporal resolution for the validation. Therefore, a combined numerical and experimental investigation of a generic space launcher model's wake flow is performed. Since each method possesses its own strengths and shortcomings, a particular focus of the presented analysis lies on a comparison between the chosen investigation techniques as well as on the importance of their combination.

2 EXPERIMENTAL APPROACH

2.1 Geometry and Flow Conditions

The simulations and measurements are performed on a generic axisymmetric space launcher model with a sting support attached to the base which mimics an endless nozzle extension and is used to mount the model in the wind tunnel as shown in Fig. 1. The space launcher model consists of a 36 degree cone with a spherical nose of $R = 5$ mm and a cylindrical main body with a length of 164.3 mm and a diameter of $d = 54$ mm. The total length, from nose to base, is 231.3 mm. The diameter of the attached sting is $d_{\text{nozzle}} = 21.5$ mm leading to the same nozzle – main body ratio of ≈ 0.4 as for Ariane 5. The analyzed

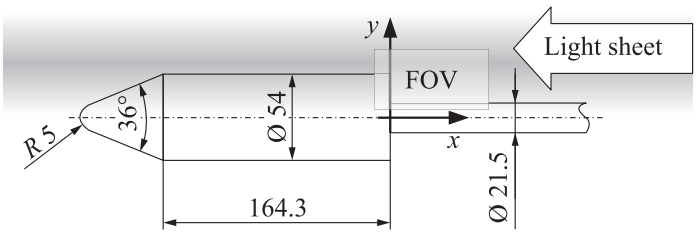

Figure 1 Axisymmetric space launcher model with rear sting. The laser light sheet and the field of view (FOV) for high-repetition rate PIV measurements are illustrated. Numerical values are given in millimeters

Table 1 Freestream conditions

Ma	Re, 1/m	U, m/s	p_0, Pa	p, Pa	T_0, K	T, K
0.7	$19 \cdot 10^6$	228	$1.5 \cdot 10^5$	$1.08 \cdot 10^5$	290	264

data sets were achieved at a Mach number of Ma = 0.7 and a Reynolds number, based on the forebody's diameter $d = 54$ mm, of $\mathrm{Re}_d = 10^6$. The corresponding set of the used freestream conditions is presented in Table 1.

2.2 High-Repetition-Rate Particle Image Velocimetry

High-repetition-rate PIV measurements were performed in the Trisonic Wind tunnel at the Bundeswehr University in Munich (TWM). The flow was seeded with DEHS (Di-Ethyl-Hexyl-Sebacat) tracer particles with a mean diameter of 1 μm. The particles in the field of view were illuminated by a 1-millimeter thick light sheet using a Quantronix Darwin Duo Nd:YLF double-pulse laser with an output energy of 11 mJ per cavity at 2 kHz and 527-nanometer wavelength. The particle images were recorded by using a *Phantom V12* high repetition rate CMOS (complementary metal–oxide–semiconductor) camera (by Vision Research Inc.) which was attached to a Makro.Planar T.2/100 objective lens (by Carl Zeiss AG) with a focal length of 100 mm and a f-number of 2.8. The image size was reduced to 1,280 × 400 px, which corresponds to 115 × 36 mm in physical space (see FOV in Fig. 1). The recording rate was set to 2 000 image pairs per second. In order to avoid bias errors due to three-dimensional (3D) effects or curved stream lines (as discussed in [4]), the motion of the particle images between successive frames was limited to 10 pixel by setting the time between the laser-pulses to 3 μs. In total, 21,500 PIV image pairs were acquired in four wind tunnel runs. More details about the measurement setup as well as on the TWM facility can be found in [5, 6].

2.3 Particle Image Velocimetry Data Evaluation

During the wind tunnel run, the model vibrates in the yz-plane (see Fig. 1) with an amplitude in the range of 1 mm. The dominant frequency of the vibration ($\approx$ 40 Hz) is much lower than the vortex shedding frequency ($\approx$ 900 Hz). In the first evaluation step, the PIV image pairs were shifted to compensate for the space launcher model's in-plane motion. This is important to keep the in-plane resolution on the level determined by the optical system because else, the resolution would be artificially lowered by the vibration of the model or measurement equipment. The out-of-plane motion cannot be corrected with the used measurement setup. However, the vibration amplitude is much smaller than the model diameter (54 mm). Thus, the out-of-plain motion is of minor importance for the accuracy of the PIV results. In the next step, the correlation function was computed for each pixel with the so-called single-pixel ensemble-correlation evaluation, as discussed in [7]. Finally, the mean velocity was estimated from the correlation peak maximum's position for each pixel with subpixel accuracy.

The shape of each correlation function also contains the information about the velocity's probability density function (PDF) of the in-plane velocity components, from which the Reynolds stresses are computed. However, in order to achieve reliable results for the higher order statistics, the correlation functions were computed with a sum-of-correlation approach with reduced resolution of 8×8 px to obtain smooth correlation functions even for the limited number of independent measurements, which was taken in the experiment. That allows for an accurate estimation of the PDF. The strong advantage of this new approach is, beside the enhanced spatial resolution, the fact that turbulent structures of all scales are considered. Even those that are smaller than the interrogation-window size are included in the Reynolds stresses and the results are no longer low-pass filtered, in contrast to state-of-the-art window correlation methods. The evaluation procedure is discussed in detail in [7].

3 COMPUTATIONAL APPROACH

The time-resolved numerical computations of the flow field around the generic space launcher configuration are performed by the Institute of Aerodynamics at the RWTH Aachen University using a zonal RANS/LES approach. The computation domain around the rocket configuration is split into a main body zone with an attached flow where the turbulent flow field is predicted by solving the RANS equations and a wake zone where the unsteady separated flow is time-resolving computed by LES.

3.1 Flow Solver

The computations are done on a structured vertex-centered multiblock grid using an in-house zonal RANS/LES finite volume flow solver. The Navier–Stokes equations of 3D unsteady compressible flow are discretized in conservative form by a mixed centered upwind AUSM (advective upstream splitting method) scheme [8] at second-order accuracy for the Euler terms and by a second-order accurate centered approximation for the viscid terms accounting for low numerical dissipation. The temporal integration is performed by an explicit 5-stage Runge–Kutta method with second-order accuracy as well. The LES formulation is based on the monotone integrated LES (MILES) approach [9] modeling the impact of the subgrid scales by numerical dissipation. A detailed description of the fundamental LES solver is given by Meinke *et al.* [10] and its convincing solution quality for fully turbulent sub- and supersonic flows is discussed by Alkishriwi *et al.* [11] and El-Askary *et al.* [12]. The RANS part is based on the same overall discretization schemes and a one-equation turbulence model of Spalart and Allmaras [13] to close the time-averaged equations.

3.2 Synthetic Turbulent Generation

The required transition from the RANS to LES zone is obtained by applying a synthetic turbulence generation (STG) method according to Roidl *et al.* [14]. In this approach, turbulent structures are generated in the inflow plane of the overlapping RANS/LES region as a superposition of coherent vortices via form functions which meet specific spatial and temporal characteristics derived from the turbulent viscosity μ_t of the upstream RANS solution. As a result, the final velocity signal is composed of an averaged velocity component $\overline{u}_i$ which is provided from the upstream RANS solution and the normalized stochastic fluctuations u_i' which are subjected to a Cholesky decomposition $a_{i,j}$ to assign the values of the Reynolds-stress tensor.

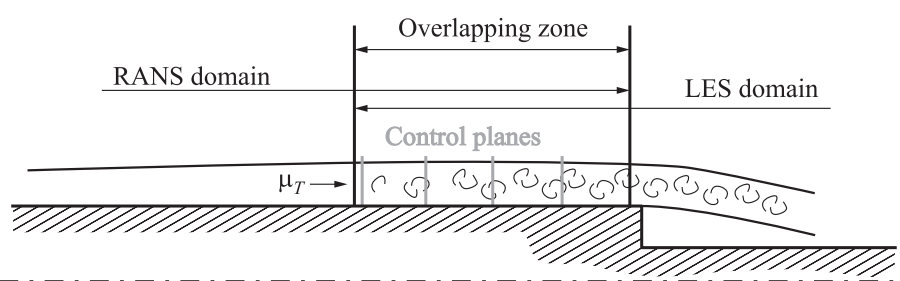

Figure 2 The RANS/LES overlapping zone with control planes

To minimize the transition zone between the RANS and LES domains, body forces f_i are added to the wall-normal momentum equation at a number of control planes at different streamwise positions to match the turbulent flow properties of the LES with the given RANS values as shown in Fig. 2. The amplitude of the force term is controlled by a proportional plus integral controller, which controls the deviation between the target and the current profile of the reconstructed Reynolds shear stresses. This approach allows the transitional length to be reduced to less than three boundary-layer thicknesses. For a detailed description of the applied zonal RANS/LES method as well as its validation against pure LES and DNS (direct numerical simulation) data for compressible flows, the reader is referred to [14].

3.3 Computational Grid

According to the applied zonal approach, the RANS domain covers the main body and the LES region encompasses the base and the sting support as shown in Fig. 3. The RANS section extends to approximately $10d$ upstream of the conical top and in the radial direction, and its downstream boundary is located at the base shoulder. The LES domain extends from $-0.5d$ to $2.5d$ in the streamwise direction with the base shoulder being the point of origin. This creates an

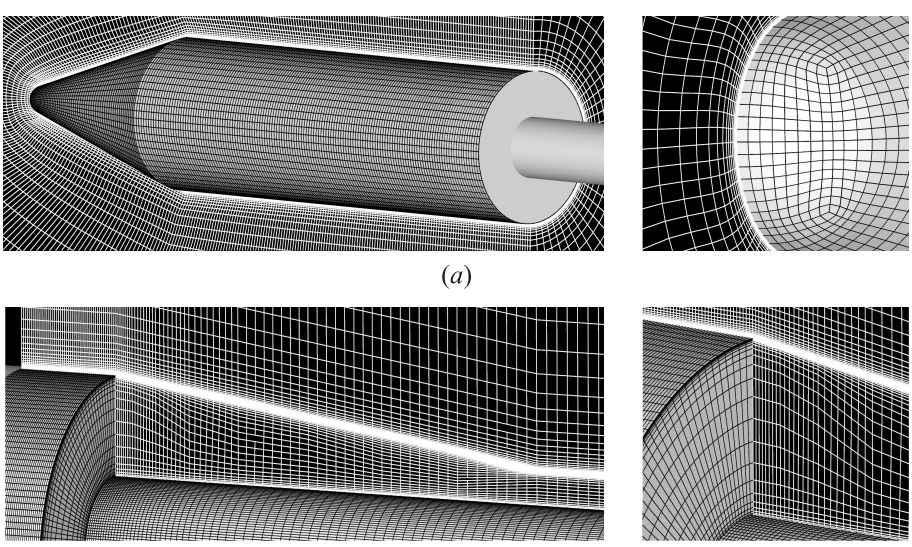

Figure 3 Computational grids for the RANS (a) and LES (b) zones

Table 2 Cell sizes at model walls in inner and outer coordinates for RANS and LES zones

Zone	$\Delta x/l^+$	$\Delta r/l^+$	$\Delta\varphi/l^+$	$\Delta r/\delta$	φ	Grid points
RANS	500	1	150	$3 \cdot 10^{-4}$	360°	$16 \cdot 10^6$
LES	50	1	40	$3 \cdot 10^{-4}$	60°	$60 \cdot 10^6$

overlapping zone of $0.5d$ upstream from the base shoulder corresponding to 5 boundary layer thicknesses, which is sufficient for the RANS/LES transition. Additional mesh refinements are realized in the regions with high gradients, e. g., along the boundary and shear layers as well as near the base shoulder. The resulting mesh parameters are summarized in Table 2. Due to the very large number of grid points required for the LES zone, a sector of 60° with periodical boundary conditions on its sides was used to compute a longer time period. The used numerical methodology and mesh resolutions are adequate to compute the separated wake flow as demonstrated in Fig. 4 illustrating a satisfactory agreement between the computed wall pressure coefficient distribution on the attached sting presented in [15] and the experimental data of Deprés *et al.* [16].

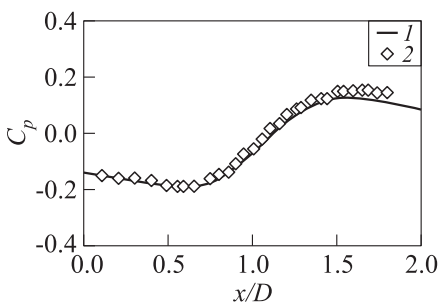

Figure 4 Comparison of the wall pressure coefficient distribution computed via zonal RANS/LES (*1*) to experimental data [16] (*2*)

4 RESULTS

The presented results are divided into four sections. First, the temporal and spatial resolution of the applied investigation techniques is analyzed in detail. Then, the time-averaged experimentally detected and numerically computed flow fields are presented and compared to each other in order to introduce the flow field topology, demonstrate the resolution of the chosen methods, and discuss the effect of different boundary conditions and model assumptions. In the third section, an analogous approach is applied with respect to the Reynolds shear stress, representing the values of velocity fluctuations. Finally, the LES results are used in order to assess the accuracy and limitations of the PIV for detection of coherent turbulent structures in the wake.

4.1 Comparison of Temporal and Spatial Resolution

Due to the strong turbulent character of the wake, the PIV and LES results should be analyzed and compared to each other with respect to the mean and fluctuating levels of the velocity as well as to the detection of relevant coherent structures. A statistically reliable analysis of the highly unsteady flow field requires a data set of sufficient time length captured at a satisfactorily high sampling frequency with high spatial resolution. However, the PIV and LES results differ significantly in this respect and therefore, their temporal and spatial resolutions must be discussed in detail.

The measurement duration of the PIV experiments in a wind tunnel was about 10 s and provided 21,500 statistically independent image pairs. On the other hand, modern PIV methods capture two image pairs at frequencies of a few kilohertz and, therefore, at high freestream velocities, usually capture completely different fluid particles and coherent structures, which makes the tracking of them in time impossible. The spatial resolution of PIV is limited by the digital particle image diameter in the direction normal to the flow direction and by the particle image displacement in streamwise direction. Both depend on the optical setup and the camera sensor. Here, the particle image diameter was ≈ 180 μm and the displacement was < 650 μm. The LES possesses a higher spatial resolution which is additionally refined in the regions with high gradients, e. g., boundary and shear layers. It also allows a time-resolved capturing of the fluid motion at any desired sampling rate, limited practically only by the necessity to store the written output data of a large size on physical media. On the other hand, even a relatively efficient zonal RANS/LES still needs a large computing time to simulate only a few milliseconds of the fluid motion, which makes a statistically reliable analysis of the computed data difficult.

To compare the time scales resolved by different techniques, a characteristical time unit $1\,t_{\mathrm{ref}} = d/U_\infty$ is introduced that denotes the time interval in which a particle moving at the freestream velocity covers a path of the length of the main body diameter. Using the freestream values of the current investigations given in Table 1, $1\,t_{\mathrm{ref}}$ corresponds to 0.24 ms and, thus, can be captured at a frequency of at least 4.2 kHz. Using this nomenclature, the PIV and LES results are compared to each other with respect to their time resolution.

In the case of the PIV experiments, the results are computed from 21,500 image pairs acquired at 2 kHz corresponding to a nondimensional reference time of $t/t_{\mathrm{ref}} = 44{,}000$ and a sampling period of $2.1\,t_{\mathrm{ref}}$. The whole ensemble of PIV image pairs is used to compute a map of correlation functions. Although no tracking of particles or coherent structures in time is possible due to the large sampling period, the PIV data provide highly accurate and reliable mean velocity field and integrative values for the velocity fluctuations as will be presented below.

The LES results are computed from 495 flow field samples written out at 42 kHz ($\widehat{=}\,0.1\,t_{\mathrm{ref}}$) corresponding to a total time interval of $t/t_{\mathrm{ref}} = 50$. Although

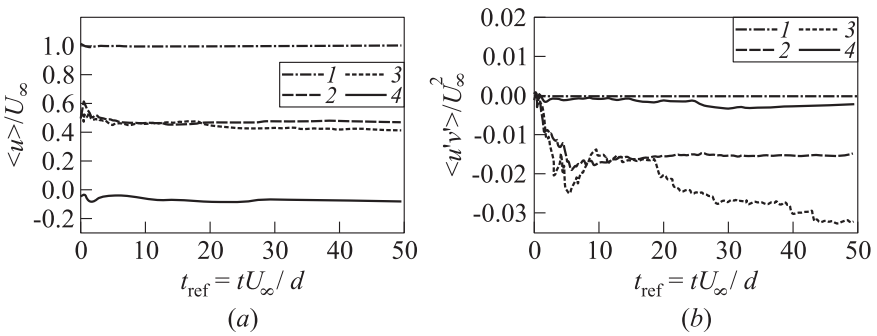

Figure 5 Flow statistics from the LES data set: absolute error of the estimated horizontal mean velocity (a) and the Reynolds shear stress (b) at characteristic locations (1 — $x = -0.1$, $y = 0.6$; 2 — $x = 0.15$, $y = 0.5$; 3 — $x = 1.0$, $y = 0.4$; and 4 — $x = 0.2$, $y = 0.3$) as a function of physical simulation time

the sampling period easily allows for tracking of relevant coherent structures, the total time is significantly shorter compared to the experiment. However, the time interval is satisfactory for a reliable statistical analysis, as shown in Fig. 5. The figure illustrates how the length of the computed signal in t_{ref} effects the estimated mean velocity (Fig. 5a) and Reynolds shear stress $\langle u'v' \rangle$ (Fig. 5b) for four characteristic points: incoming boundary layer, first part of the separated shear layer, developed shear layer, and inside the primary recirculation region. For reliable predictions of the mean velocity, a time interval of approximately $20\, t_{\text{ref}}$ can be considered as sufficient since the deviation of U_∞ within $20 < t_{\text{ref}} < 50$ is about $\pm 1.5\%$. The estimation of the Reynolds shear stress in the incoming boundary layer (1) and inside the primary recirculation region (4) as well as in the first part of the separated shear layer (2) is satisfactorily accurate with a time interval of $30\, t_{\text{ref}}$. For regions within the developed shear layer (3), the interval length of $50\, t_{\text{ref}}$ is though acceptable, a sequence of a longer length would be, however, more appropriate for a more reliable statistical results for the Reynolds stress tensor.

4.2 Mean Velocity Distribution

The mean velocity distribution (normalized by $U_\infty = 228$ m/s) in the plane of symmetry of the space launcher model's wake is shown in Fig. 6 for the PIV and LES, respectively. The axisymmetric backward facing step at $x/d = 0$ causes a strong separation of the incoming highly turbulent boundary layer leading to a formation of a low-pressure region downstream of the base. As a result, the shear layer sheds from the shoulder of the cylindrical forebody and broadens further downstream because of turbulent mixing effects. Due to the low-pressure

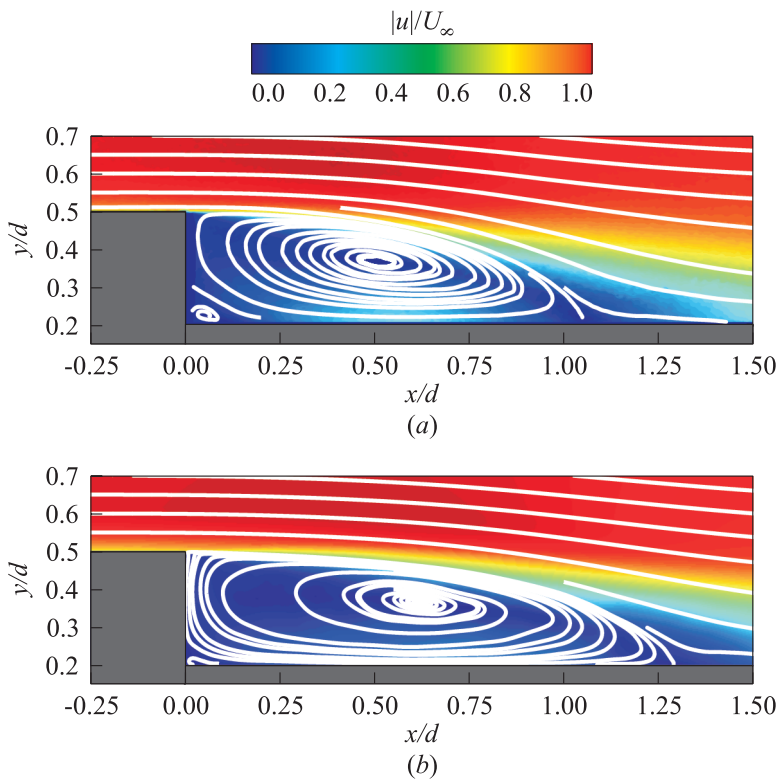

Figure 6 Comparison of the mean velocity distribution in the space launcher model's wake estimated using experimental PIV images (a) and LES (b)

region at the base, the shear layer is deflected towards the sting and reattaches on it forming a closed recirculation zone.

Inside the recirculation zone, the streamlines of the mean wake flow in Fig. 6 clearly show an out-of-plane motion within the recirculation region; the lines do not form closed loops but they bend outwards (for LES) or inwards (for PIV) indicating a source or a drain in the plane of symmetry at $x/d \approx 0.60$ and $y/d \approx 0.37$ and at $x/d \approx 0.51$ and $y/d \approx 0.37$ for LES and PIV, respectively. This indicates a 3D motion of fluid with a nonzero component in azimuthal direction. In the corner of the primary recirculation region, a secondary recirculation region appears in the mean flow field.

One notices the differences between the experimental measurements and numerical computations, particularly, in respect of the reattachment length, i. e., $x_\mathrm{r}/d = 1.06$ and 1.30 for the experiment and simulation, respectively. After cross-checking the experimental and numerical data and parameters, it was found

that one of the possible reasons for the deviations are the differences in turbulence intensity of the flow incoming at the model shoulder. This fact is illustrated in Fig. 7 showing a comparison of the velocity profiles of the incoming boundary layers for PIV and LES at $x/D = -0.1$. First, the nonuniform grid of LES allows for the resolution of all relevant scales down to the viscous sublayer, whereas the PIV resolution cannot be refined in regions with strong gradients and the resolution in the near-wall region is limited by the particle image size [17, 18]. Thus, PIV resolves the profile only down to the logarithmic layer. However, it can be already seen from the figure that the velocity in the logarithmic layer is larger in the experiment compared to the simulations indicating a larger turbulence level in the experiment. The resulting values for boundary layer thickness δ_{99}, displacement thickness δ_1, momentum thickness δ_2, and shape factor H_{12} are summarized in Table 3 for the numerical and experimental approach. The higher turbulence level in the experimental results might be a result of tiny model vibration with an amplitude and frequency of ± 1 mm and ≈ 37 Hz during the wind tunnel run [5]. These vibrations may cause a tiny unsteady flow separation at the shoulder of the main body. However, also a higher turbulence level of the wind tunnel than assumed in the computation may explain the difference between experiment and simulation.

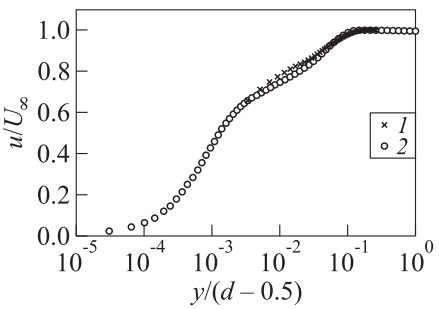

Figure 7 Incoming boundary layer: *1* — single-pixel PIV; and *2* — LES

Table 3 Parameters of boundary layer profiles

Method	δ_{99}/d	δ_1/d	δ_2/d	H_{12}
LES	0.100 ± 0.005	≈ 0.0086	≈ 0.0056	≈ 1.53
PIV	0.120 ± 0.005	> 0.0106	> 0.0091	≈ 1.17

4.3 Reynolds Shear Stress

Figure 8 shows the spatial distribution of the Reynolds shear stress $\langle u'v' \rangle$ (normalized by the mass density and the free stream velocity squared) as a commonly used indicator of the turbulence production in the xy-plane for the computational and the experimental approach, respectively. The topology is quite similar, but there are differences in intensity of Reynolds shear stress between the measurements and computations which might be caused by differences between the in-

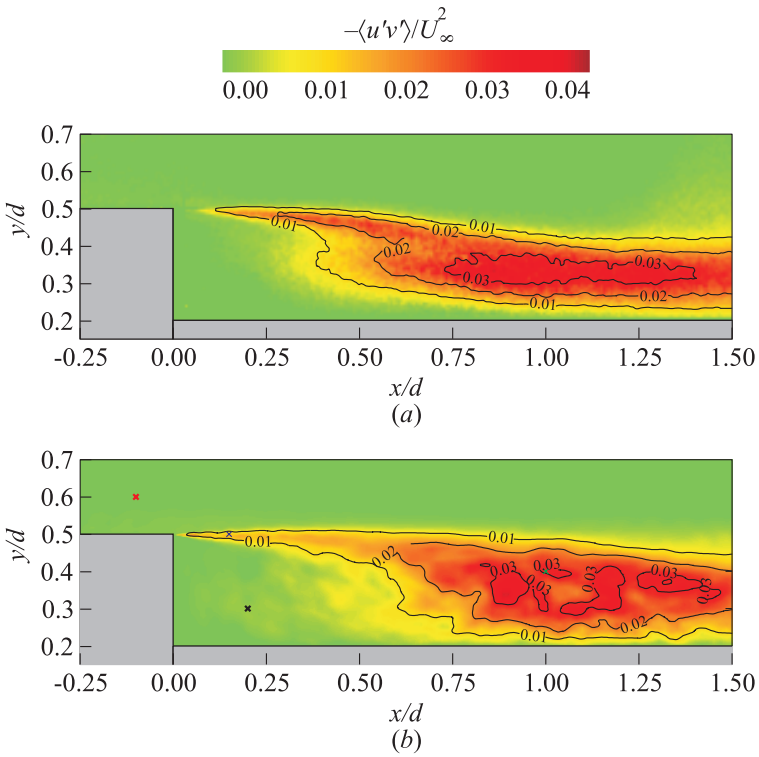

Figure 8 Comparison of the mean velocity distribution in the space launcher model's wake estimated using experimental PIV images (a) and LES (b)

coming boundary layer, as already discussed in the previous section. As a result, the overall stress distribution differs significantly in the following points:

(1) for LES, the shear stress rises very fast in the first part of the separated shear layer to a value of $-\langle u'v'\rangle \approx 0.015U_\infty^2$ but is fairly constant for $0.1 < x/d < 0.6$;

(2) for PIV, the stress values in the shear layer increase continuously until $x/d \approx 0.5$;

(3) the curvature of the upper part of the 0.01 iso-line is of different sign for LES and PIV at $0.75 < x/d < 1.25$;

(4) downstream of reattachment, the shear layer is thicker in the case of LES compared to PIV; and

(5) the PIV results are characterized by secondary local maximum within the primary recirculation region at $0.3 < x/d < 0.6$ and $y/d \approx 0.35$, which is not (clearly) visible in the case of the LES approach.

The first four points can be traced back to the previously discussed different level of turbulence in the incoming flow or the tiny vibrations of the wind tunnel model due to the high load of the model at Ma = 0.7. The latter are believed to trigger and amplify the flapping motion of the shed shear layer leading to a stronger turbulent mixing between the slow recirculation zone and fast outer flow. The last point is likely to be caused by the total signal length of the LES of $50\,t_{\mathrm{ref}}$ as was shown in Fig. 5.

4.4 Shear Layer Vortices

The interaction between the shedding shear layer vortices and the main engine's nozzle reaches its maxima at transonic speeds and leads to strongly increased mechanical loads on the nozzle structure, which is broadly known as buffeting. Therefore, the accuracy of the detection of the shear layer vortices as well as of tracking their formation and motion in the separated region is vital for the understanding, prediction, and control of the buffeting phenomena. To illustrate the capabilities of the LES and PIV to satisfactorily resolve the coherent structures of relevant scales, the vortices in the wake of the investigated configuration are identified and analyzed from instantaneous snap shots of the flow field provided by both techniques using the same postprocessing algorithm and different spatial resolutions.

For the large-eddy simulation, 495 velocity fields in the plane of symmetry, each consisting of 27 800 data points, are considered. Figure 9*a* shows a characteristic snapshot of the vortex distribution in the space launcher model's wake. The nonreal eigenvalues of the velocity gradient matrix

$$\frac{\partial \vec{v}}{\partial \vec{x}} = \begin{pmatrix} u_x & u_y \\ v_x & v_y \end{pmatrix} = \begin{pmatrix} \dfrac{\partial u}{\partial x} & \dfrac{\partial u}{\partial y} \\ \dfrac{\partial v}{\partial x} & \dfrac{\partial v}{\partial y} \end{pmatrix}$$

are used to detect the vortices [19–21]. The discriminant

$$D_2 = \left(\operatorname{trace} \frac{\partial \vec{v}}{\partial \vec{x}} \right)^2 - 4 \det \frac{\partial \vec{v}}{\partial \vec{x}} = (u_x + v_y)^2 - 4\,(u_x v_y - u_y v_x)$$

of the velocity gradient matrix is negative for vortices and positive for other patterns. In order to detect the shear layer vortices, the swirling strength swirl of the vector fields is computed as follows:

$$\mathrm{swirl} = \max\,(0; -D_2)\,\mathrm{sign}\,(\omega_z)$$

where swirl is the negative part of the discriminant of the velocity gradient matrix multiplied by the sign of the vorticity ω_z, which allows for the determination

of the rotation direction: negative swirling strength corresponds to clockwise rotation and positive swirling strength corresponds to counterclockwise rotation. To account for the nonaxisymmetric shape that appears if the vortex tube axis is not aligned perpendicular to the measurement plane, the swirling distribution is analyzed locally by a Gaussian with elliptical cross section.

More than 200 vortices are detected in each LES velocity field. Very small ones with very high swirling strength are generated at the point of separation. These vortices grow in size while traveling downstream resulting in a decreased swirling strength. A large majority of the vortices have a negative swirling strength, which corresponds to a clockwise rotation direction, which is expected from the model's geometry and the flow direction. On the other hand, a significant fraction of the vortices has a counterclockwise rotation direction. These vortices are not generated from the separation at the end of the cylindrical main body but from the clockwise rotating vortices. The counterclockwise rotating vortices are significantly smaller than the clockwise rotating ones and they appear mainly in the developed shear layer and close to the models rear sting. This findings are consistent with experimetal results in the case of a two–dimensional backward facing step flow presented by Scarano *et al.* [22].

The PIV measurements yield 21,500 vector fields with $160 \times 50 = 8{,}000$ data points on a regular grid. Standard window cross correlation, including window shifting and image deformation, was applied to compute the instantaneous vector fields resulting in reduced resolution and accuracy, compared to ensemble-averaged PIV evaluation techniques. The spatial resolution (distance between independent vectors) is $\approx 0.05d$, which is not sufficient to resolve the small shear layer vortices. Therefore, only the largest and strongest vortices are detected. The vortex distribution for a characteristic velocity field is shown in Fig. 9*b* and differs significantly from the LES vortex field discussed above, which is, however, basically caused by the coarser spatial resolution and is proved as follows. The LES resolution can be artificially reduced to the PIV value by averaging over a window of $0.05d \times 0.05d$. The vortices detected in this artificially coarser LES field are shown in Fig. 9*c* for the same vector field as in Fig. 9*a*. Like for the PIV case, only a small fraction of the vortices, the largest and strongest ones, are detected in the case of reduced resolution. Since the counterclockwise rotating vortices are smaller in size, most of them disappeared. Moreover, due to the coarser resolution, an artificial vortex agglomeration occurred. This means that the size of small vortices is overestimated and multiple neighboring vortices are wrongly detected as one larger vortex.

Taking into account the vortex agglomeration aspect due to a coarser resolution mentioned above, both investigation techniques are compared to each other with respect to the vortex size detection. A corresponding histogram of the major axis length L_1 of the cross section of the detected vortices is shown in Fig. 10. For the LES data, the vortex size with highest probability is around 0.01 times the main body diameter, whereas for the PIV data, this value is about $0.08d$ due

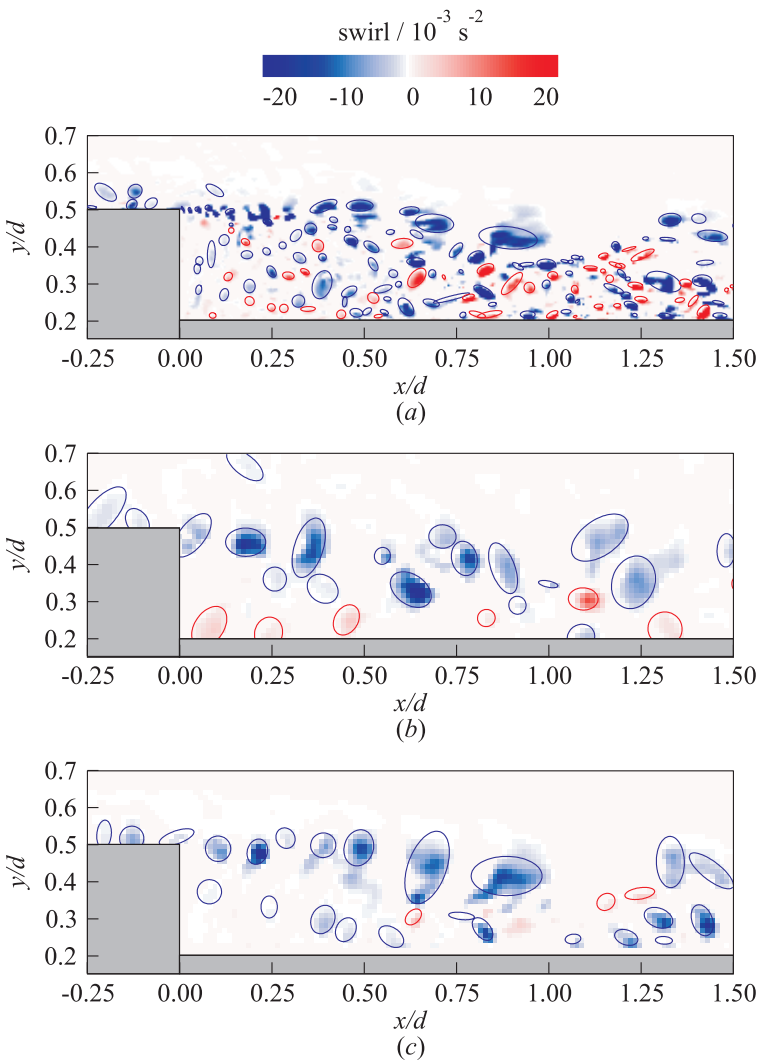

Figure 9 Characteristic vortex distribution in the space launcher model's wake for LES (a), for an experimental PIV velocity field (b), and for artificially coarse LES matching the PIV resolution (c)

to the limited resolution of the PIV approach. In the case of artificial reduction of the LES resolution, the histogram is strongly shifted to larger vortex size as indicated by curve *3* in Fig. 10. Thus, the approach wrongly identifies several vortices of much larger size, featuring a maximum around $L_1/d = 0.05$ instead of 0.01 at

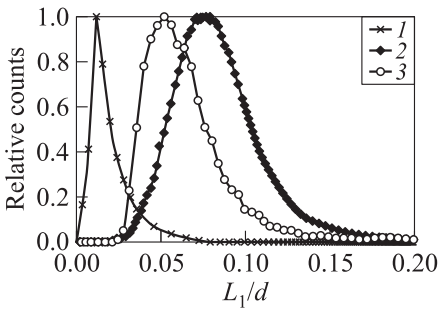

Figure 10 Histogram of the vortex size distribution for detected vortices from LES data (*1*), from PIV data (*2*), and from averaged LES data (*3*)

the original LES resolution. The artificially coarser LES, however, still detects smaller vortices than the PIV which should be traced back to the larger turbulence level and stronger turbulent mixing in the experiment indicated previously as well to the measurement noise which complicates the detection of small vortices. Thus, an analysis of the vortices should be based on the LES results as the classical PIV resolution is not sufficient to detect the vortices and their geometry without bias errors.

5 CONCLUDING REMARKS

The performed experimental and numerical investigation of the transonic wake of the generic axisymmetric space launcher model revealed versatile findings. It was shown that the LES is characterized by a very large temporal and spatial resolution which is ideally suited for the computation of the highly turbulent wake with regions of flow separation and can reliably be used for the detection of all relevant coherent structures as well as for tracking their motion in time. On the other hand, although the zonal RANS/LES approach is more efficient than the pure LES, the computations still need to be done on high-performance computers using hundreds of cores and usually take several months. Furthermore, the finally computed physical time span capture only several large-wave periods of the flow motion, which can be critical for statistical analysis of results, grid convergence, and parameter studies.

On the other hand, the high-repetition-rate PIV approach results in a much larger ensemble of statistically independent measurements with a spatial resolution adequate for a reliable estimation of flow statistics. However, the PIV resolution for instantaneous velocity fields is rather coarse as conventional correlation techniques must be applied. As a result, only large coherent structures can be detected in the instantaneous velocity fields and some of them are just an agglomeration of originally smaller vortices that cannot be distinguished apart. This conclusion could only be drawn by comparing the original and artificially coarser LES results. It was shown that the reason why the PIV and LES results slightly differ from each other in terms of the length of the recirculation region and the level of velocity fluctuations was a difference in turbulent intensity of the incoming boundary layer. This was most likely caused by model vibrations

during the experiment and a different turbulence level of the free stream flow. Putting together the strength of the numerical and experimental technique, it is possible to get a quite complete picture of the flow physics. Furthermore, it becomes possible to detect regions of the flow where special care must be taken with the validity of each technique. Finally, the investigation shows that the accuracy of the sophisticated experimental and numerical technique is sufficiently developed for such investigations. However, the definition and preparation of conserved boundary conditions require more attention in the future.

ACKNOWLEDGMENTS

Financial support from the German Research Foundation (Deutsche Forschungsgemeinschaft — DFG) in the framework of the Sonderforschungsbereich Transregio 40 is gratefully acknowledged by the authors. Computational resources have been provided by the Stuttgart High-Performance Computing Center (HLRS).

REFERENCES

1. Lüdeke H., J. B. Calvo, and A. Filimon. 2006. Fluid structure interaction at the Ariane-5 nozzle section by advanced turbulence models. *European Conference on Computational Fluid Dynamics — ECCOMAS CFD*. The Netherlands: TU Delft.
2. Hannemann, K., H. Lüdeke, J. F. Pallegoix, A. Ollivier, H. Lambaré, J. E. J. Maseland, E. Geurts, M. Frey, S. Deck, F. F. J. Schrijer, F. Scarano, and R. Schwane. 2011. Launcher vehicle base buffeting — recent experimental and numerical investigations. *7th European Symposium on Aerothermodynamics for Space Vehicles Proceedings*. Brugge, Belgium.
3. Schrijer, F. F. J., A. Sciacchitano, F. Scarano, K. Hanneman, J. F. Pallegoix, J. E. J. Maseland, and R. Schwane. 2011. Experimental investigation of base flow buffeting on the Ariane 5 launcher using high speed PIV. *7th European Symposium on Aerothermodynamics for Space Vehicles Proceedings*. Brugge, Belgium. 692:102.
4. Scharnowski, S., and C. J. Kähler. 2013. On the effect of curved streamlines on the accuracy of PIV vector fields. *Exp. Fluids* 54:1435.
5. Bitter, M., S. Scharnowski, R. Hain, and C. J. Kähler. 2011. High-repetition-rate PIV investigations on a generic rocket model in sub- and supersonic flows. *Exp. Fluids* 50:1019–1030.
6. Bitter, M., T. Hara, R. Hain, D. Yorita, K. Asai, and C. J. Kähler. 2012. Characterization of pressure dynamics in an axisymmetric separating/reattaching flow using fast-responding pressure-sensitive paint. *Exp. Fluids* 53:1737–1749.
7. Scharnowski, S., R. Hain, and C. J. Kähler. 2012. Reynolds stress estimation up to single-pixel resolution using PIV-measurements. *Exp. Fluids* 52:985–1002.
8. Liou, M.-S., and C. J. Steffen. 1993. A new flux splitting scheme. *J. Comput. Phys.* 107:23–39.

9. Boris, J., F. Grinstein, E. Oran, and R. Kolbe. 1992. New insights into large eddy simulation. *Fluid Dyn. Res.* 10:199–228.
10. Meinke, M., W. Schröder, E. Krause, and Th. Rister. 2002. A Comparison of second- and sixth-order methods for large-eddy simulations. *Comput. Fluids* 31:695–718.
11. Alkishriwi, N., M. Meinke, and W. Schröder. 2006. A large-eddy simulation method for low Mach number flows using preconditioning and multigrid. *Comput. Fluids* 35(10):1126–1136.
12. El-Askary, W. A., W. Schröder, and M. Meinke. 2003. LES of compressible wall-bounded flows. AIAA Paper No. 2003-3554.
13. Spalart, P. R., and S. R. Allmaras. 1992. a one-equation turbulence model for aerodynamic flows. AIAA Paper No. 92-0439.
14. Roidl, B., M. Meinke, and W. Schröder. 2012. A zonal RANS–LES method for compressible flows. *Comput. Fluids* 67:1–15.
15. Statnikov, V., C. Glatzer, J.-H. Meiß, M. Meinke, and W. Schröder. 2013. Numerical investigation of the near wake of generic space launcher systems at transonic and supersonic flows. *Progress in flight physics*. Eds. Ph. Reijasse, D. D. Knight, M. S. Ivanov, and I. I. Lipatnikov. EUCASS advances in aerospace sciences book ser. 5:191–208.
16. Deprés, D., P. Reijasse, and J. P. Dussauge. 2004. Analysis of unsteadiness in afterbody transonic flows. *AIAA J.* 42:2541–2550.
17. Kähler, C. J., S. Scharnowski, and C. Cierpka. 2012. On the uncertainty of digital PIV and PTV near walls. *Exp. Fluids* 52:1641–1656.
18. Cierpka, C., S. Scharnowski, and C. J. Kähler. 2013. Parallax correction for precise near-wall flow investigations using particle imaging. *Appl. Opt.* 52:2923–2931.
19. Chong, M. S., A. E. Perry, and B. J. Cantwell. 1990. A general classification of three-dimensional flow fields. *Phys. Fluids* 2:765–777.
20. Adrian, R. J., K. T. Christensen, and Z. C. Liu. 2000. Analysis and interpretation of instantaneous turbulent velocity fields. *Exp. Fluids* 29:275–290.
21. Vollmers, H. 2001. Detection of vortices and quantitative evaluation of their main parameters from experimental velocity data. *Meas. Sci. Technol.* 12:1199–1207.
22. Scarano, F., C. Benocci, and M. L. Riethmuller. 1999. Pattern recognition analysis of the turbulent flow past a backward facing step. *Phys. Fluids* 11:3808.